Supplementary Information (SI) for ChemComm.


Supplemental Information for

# Aerogel-Inspired Interfacial Engineering of Metal-Organic Framework and Black Phosphorus Heterojunction for Enhanced $CO_2$ Photocatalytic Reduction

*Zunbin Duan[a,†], Jenaidullah Batur[b,†], Huiming Zhang[c], Yanfang Li[a], Rui Li[b,*], and Guanglei Zhang[a,*]*

[a] National Engineering Research Center for Colloidal Materials and School of Chemistry and Chemical Engineering, Shandong University, Jinan 250100, China

[b] Beijing Key Laboratory for Green Catalysis and Separation, College of Materials Science and Engineering, Beijing University of Technology, Beijing 100124, China

[c] College of Chemical Engineering and Materials, Shandong University of Aeronautics, Binzhou 256603, China

* Corresponding authors: lirui1@bjut.edu.cn (R. Li) and zhanggl@sdu.edu.cn (G. Zhang)

[†] Both authors contributed equally to this work

## SECTION S1. Experimental Procedures

### *S1.1 Materials*

Black phosphorus (BP; 99.999%) crystal was purchased from Hubei Xingfa Chemicals Group Co., Ltd. *N, N*-dimethylformamide (DMF; 99.9%), tetrabutylammonium bromide (99.5%), zirconium tetrachloride ($ZrCl_4$; 99%), 2-aminoterephthalic acid, and acetic acid were purchased from Shanghai Aladdin Biochemical Technology Co., Ltd. All chemical reagents were used as received without further purification.

### *S1.2 Synthesis of black phosphorus and metal organic framework heterojunctions*

*Synthesis of black phosphorus (BP) nanosheets by electrochemical exfoliation.*[1] The bulk BP crystals (cathode) and platinum foil (anode) were meticulously positioned in parallel separated by a distance of 5 cm, and immersed in DMF containing 40 g $L^{-1}$ of tetrabutylammonium bromide. The exfoliation process was conducted under constant current conditions of 30 mA for a duration of 30 min. The product was collected, centrifuged four times with acetone to get rid of the remaining solvent, and concentrated, yielding a suspension with a concentration of 15 mg $mL^{-1}$.

*Synthesis of metal-organic framework (MOF) by solvothermal strategy.*[2] Typically, 15.0 g (64.4 mmol) of $ZrCl_4$, 11.7 g (64.4 mmol) of 2-aminoterephthalic acid and 440 mL (7.73 mol) of acetic acid were dissolved in 1 L of DMF. Then, 75 mL of $H_2O$ was added. The resulting homogeneous solution was heated at 120 °C for 15 min under stirring before it was cooled to RT. The product of Zr-based MOF ($NH_2$-UiO-66) was separated *via* centrifugation at 10,000 rpm for 3 min and purified with ethanol several times.

*Synthesis of MOF and BP heterojunction (MOF-BP) by mechanochemical ball milling.*[1, 3, 4]

The synthesis of MOF-BP was conducted in a 50 mL agate jar, to which 27 g of agate balls, 2 mL of ethanol, and 350 mg of MOF and BP with a mass ratio of 2:1 were added. The ball-milling procedure was performed at 200 rpm for a total of 12 h, using a cyclic rotation pattern consisting of 30 min forward rotation, 30 min reverse rotation, and a 2 min pause, resulting in an overall time of 766 min. Subsequent to milling process, the resulting material was collected and dried under vacuum at 60 °C. The MOF-BP powder was subsequently stored in a sealed tube within a nitrogen-filled glovebox to prevent exposure to oxygen and oxidation.

### *S1.3 $CO_2$ photocatalytic reduction*[5]

Typically, 1 mg of photocatalyst, 20 μL of $H_2O$, and 20 μL of triethanolamine were added a 120 mL of quartz reactor without the employment of any photosensitizers. Irradiated by a xenon lamp (300 W; >400 nm), the gaseous products were evaluated every 2 h using a gas chromatograph (Agilent 7890B) with a thermal conductivity detector and helium as the carrier gas.

### *S1.4 Materials characterization*

Scanning electron microscopy (SEM) was and energy dispersive X-ray spectroscopy (EDS) were carried out on a Zeiss Supra 55 Sapphire field-emission scanning electron microscope) at 2.0 kV and a distance of 5.0 mm. Powder X-ray diffraction (XRD) was performed on a Rigaku SmartLab diffractometer by using Cu K*α* radiation (40 kV, 30 mA). X-ray photoelectron spectroscopy (XPS) was carried out on a Thermo Fisher ESCALab 250Xi spectrometer with Al K*α* radiation, and the obtained spectra were calibrated based on the C *1s* peak at 284.6 eV. The Brunauer-Emmett-Teller measurements were recorded with a Micromeritics ASAP 2020 surface area and porosimetry analyzer. The diffuse reflectance spectra were acquired on the Perkin-Elmer lambda 950 UV/Vis/NIR spectrophotometer at a scanning rate of 600 nm $min^{-1}$ and data interval of 1.00 nm. The atomic force microscopy samples were prepared by spin-coating or drop-casting an aliquot of the diluted sample-ethanol suspension on Si. The femtosecond transient absorption spectroscopy was measured by a specialized spectrometer comprised of a regenerative-amplified Ti laser system (Coherent) and a Helios pump-probe system (Ultrafast Systems). *In-situ* diffuse reflectance Fourier transform infrared spectroscopy was carried out on a Fourier transform infrared spectrometer equipped with a mercury cadmium telluride detector.

***S1.5 Photoelectrochemical measurements***

Electrochemical impedance spectroscopy (EIS) and Mott-Schottky analysis were conducted utilizing a Zahner Zennium electrochemical workstation to characterize the electrochemical properties of the photocatalyst. 2 mg of photocatalyst was dispersed in a mixed solvent comprising 1 mL of methanol and 10 μL of Nafion. Subsequent to ultrasonic dispersion, 100 μL of this suspension was deposited onto a fluorine-doped tin oxide glass substrate, thereby preparing the working electrode. The three-electrode configuration was adopted, including a Pt plate serving as the counter electrode, a Ag/AgCl electrode acting as the reference electrode, and a 0.5 M $Na_2SO_4$ solution as the electrolyte. Temporal photo-response measurements were carried out at 0.5 V. Electrochemical impedance spectroscopy was measured without light irradiation at open circuit potential. Photocurrent measurements were executed on a CHI760E electrochemical workstation, employing a 300 W xenon lamp equipped with a UV cutoff filter ($\lambda > 400$ nm) as the light source. The photocurrent response of the sample was recorded at the open circuit potential over a duration of 1,000 s to ascertain the photoelectrochemical performance. Mott-Schottky plots with frequencies of 500, 1,000, and 1,500 Hz were gathered in the voltage range of -0.8−1.0 V. All the measured voltages were converted with respect to the normal hydrogen electrode (NHE) using the Nernst equation as follows:

$$E_{NHE} = E_{Ag/AgCl} + 0.2046 \qquad (1)$$

where $E_{NHE}$ was the converted potential *vs.* NHE, $E_{Ag/AgCl}$ was the measured potential *vs.* the reference electrode of Ag/AgCl, and pH was kept at 7.0 at 25 °C.

The solar-to-chemical conversion (SCC) efficiency was obtained according to Eq. S2,

$$\text{SCC efficiency (\%)} = \frac{[\Delta G^{o}\text{for CO formation (J mol}^{-1})]\times[\text{CO formed (mol)}]}{[\text{Total input energy (W)}]\times[\text{Reaction time (s)}]}\times 100\% \qquad (2)$$

where the free energy for CO formation is 137.2 kJ $mol^{-1}$; the light intensity is 1472 mW $cm^{-2}$, and the irradiation area is $1.59 \times 10^{-1}$ $cm^2$, thus the total input energy is 0.234 W.

## SECTION S2. Supplemental figures

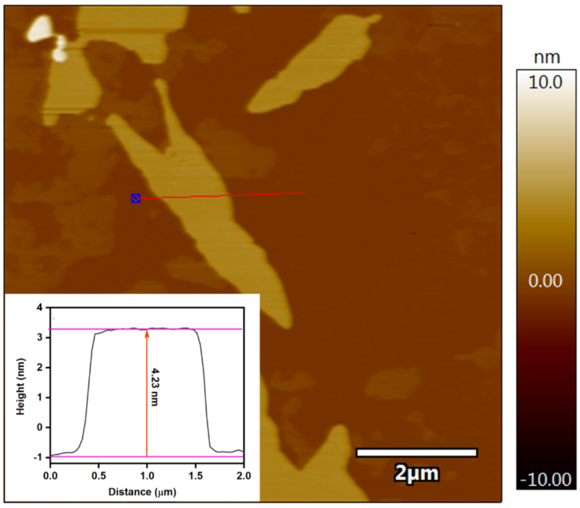


**Figure S1.** AFM image of BP sheets with an insert of measured height profile.

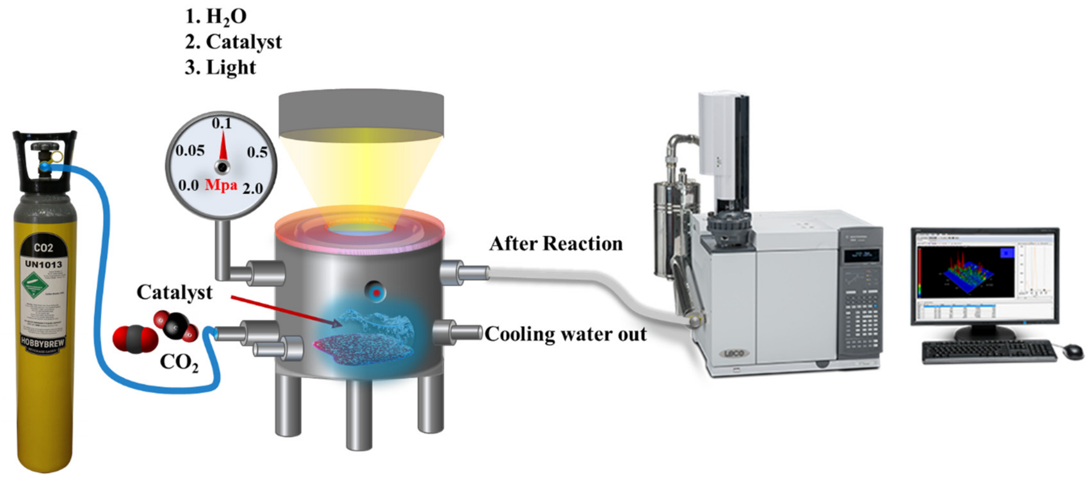


**Figure S2.** Scheme of photocatalytic process using MOF-BP catalyst.

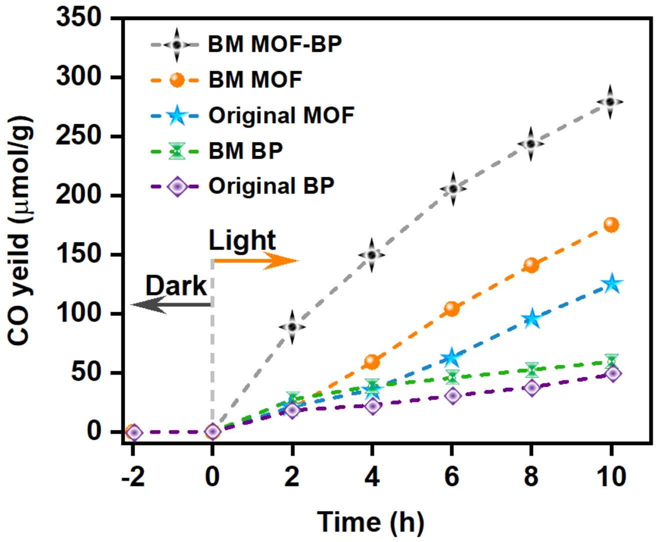


**Figure S3. Impacts of wet ball milling treatment on the photocatalytic $CO_2$RR performance.** Without ball milling (BM), the performances of $NH_2$-UiO-66 and BP are notably more inferior, exhibiting CO generation rates of only 13.3 and 3.8 μmol $g^{-1}$ $h^{-1}$, respectively. The pristine $NH_2$-UiO-66 possesses inherent photocatalytic activity, owing to its amine groups and coordinatively unsaturated $Zr^{4+}$ sites (defects), which contribute both $CO_2$ adsorption capacity and baseline $CO_2$RR activity. This explains why pristine MOF exhibits higher activity than pristine BP. In the composite system, however, the functional roles are optimized through synergistic division of labor: MOF primarily acts to adsorb and enrich $CO_2$ while supplying photogenerated electrons; BP, with its high electrical conductivity and favorable band position, efficiently accepts electrons and performs the $CO_2$-to-CO reduction step. Thus, the heterojunction overcomes the intrinsic limitations of each component (poor charge separation in MOF and weak $CO_2$ affinity in BP) and achieves much higher overall activity than either material alone. Without ball milling, the composite cannot be effectively formed and would simply correspond to a physical mixture of the two precursors.

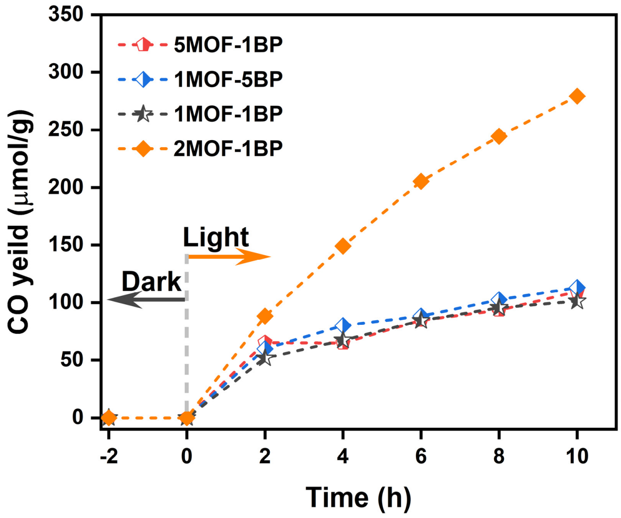


**Figure S4. Photocatalytic properties of heterojunctions composed of different MOF and BP ratios.** The heterojunctions with a mass ratio of MOF to BP of 1:5, 1:1, 2:1, and 5:1 are labeled as 1MOF-5BP, 1MOF-1BP, 2MOF-1BP, and 5MOF-1BP, respectively. The 2MOF-1BP demonstrates the optimal CO yield among the four examined photocatalysts. A specific description is not provided; the acronym MOF-BP is an abbreviation for 2MOF-1BP.

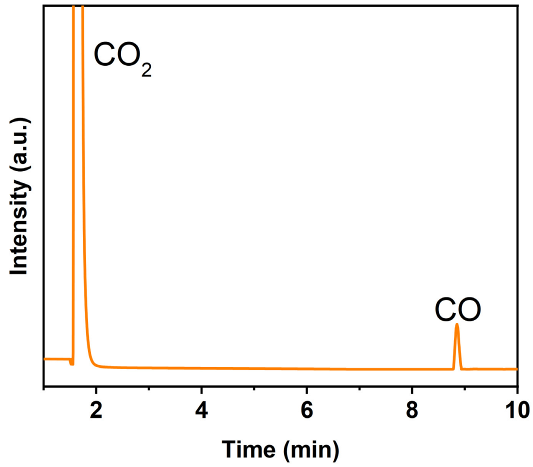


**Figure S5. Representative gas chromatogram of product.** Besides the distinct peaks correspond to $CO_2$ and CO, no detectable signals for $H_2$, other C1 (*e.g.*, $CH_4$, HCOOH), or C2 hydrocarbons (*e.g.*, $C_2H_4$, $C_2H_6$) are observed. The photocatalytic reaction for the MOF-BP proceeds through a highly selective single-carbon pathway, yielding CO as the exclusive gaseous product with a selectivity approaching 100%.

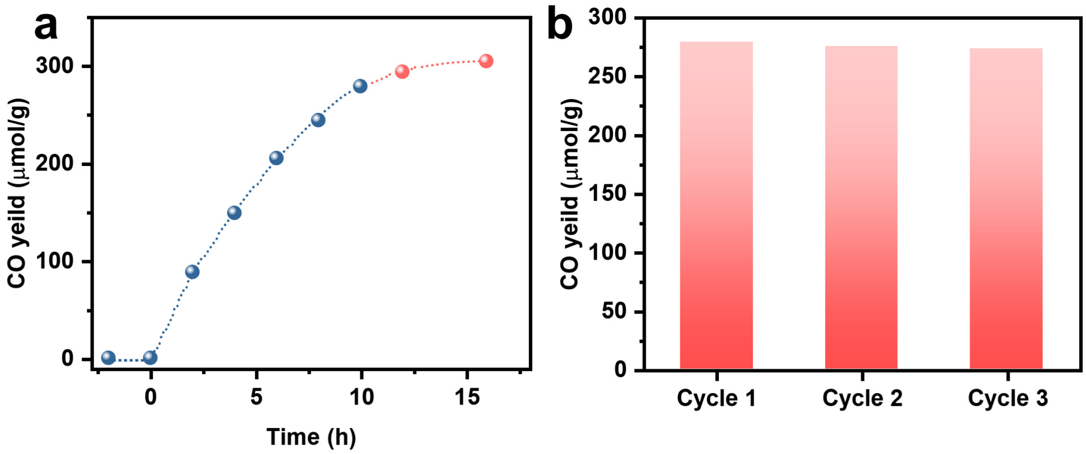


**Figure S6. (a) Long-term stability and (b) reusability of MOF-BP.** The reaction rate slows at extended irradiation times due to the depletion of available reactants in the closed reaction system (Figure S6a). After replenishing the substrate, the catalyst maintains its activity without noticeable decay, and its photocatalytic performance remains essentially unchanged over three consecutive reaction cycles (Figure S6b). Thus, the MOF-BP heterojunction possesses outstanding long-term stability and reusability for $CO_2$ photoreduction.

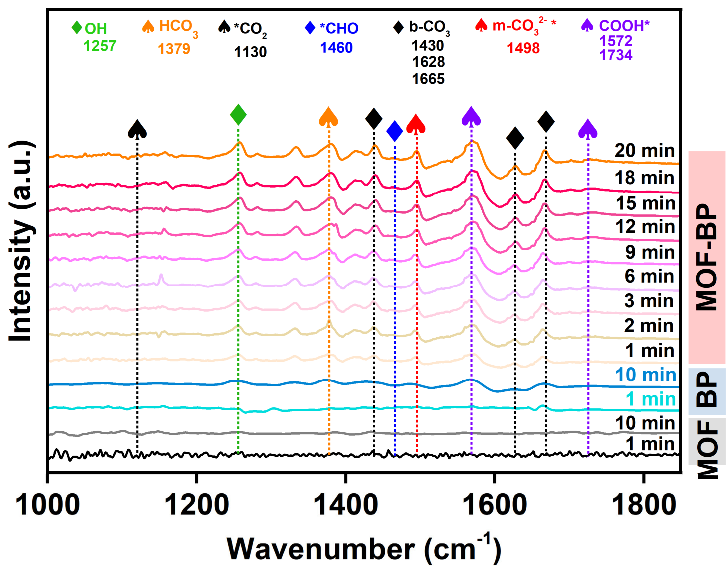


**Figure S7.** ***In-situ*** **DRIFTS spectra of MOF, BP, and MOF-BP.** The *in-situ* DRIFTS reveals radically improved signals for the designed MOF-BP, whereas the corresponding spectra of both components basically show no noticeable peaks. For MOF-BP, adsorbed $*CO_2$ and various carbonates including m-$CO_3^{2-}$, b-$CO_3^{2-}$, and $HCO_3^-$ are identified, and pivotal C1 intermediates (COOH* and *CHO) are concurrently observed, confirming its single-carbon reduction pathway for facilitating $CO_2$RR.

## SECTION S3. Supplemental tables

**Table S1.** Comparisons of MOF-BP and reported catalysts for $CO_2$ photocatalytic reduction.

| Photocatalyst | Reaction condition | Product ($\mu$mol $g^{-1}$ $h^{-1}$) | Ref. |
|---|---|---|---|
| MOF-BP | 20 L $H_2O$ and TEOA, 300 W Xe lamp ($\lambda$ > 400 nm), 10% $CO_2$ | CO: 30.7 | This work |
| MAF-34-CoRu | $CH_3CN/H_2O$ (5 mL), 300 W Xe lamp ($\lambda$ > 400 nm), 15% $CO_2$ | CO: 4.26<br>$CH_4$: 0.20 | *J. Am. Chem. Soc.* **2022***, 144,* 8676 |
| RP-MIL101 | 20 L $H_2O$ and TEOA, 300 W Xe lamp ($\lambda$ > 400 nm), 10% $CO_2/N_2$ | CO: 7.80<br>$C_2H_6$: 3.81 | *Appl. Catal. B-Environ. Energy* **2025***, 378,* 125568 |
| $MgCo_2O_4$ | 7.5 mg $[Ru(bpy)_3]Cl_2·6H_2O$ (bpy=2′2-bipyridine), 2 mL water, 3 mL acetonitrile and 1mL triethanolamine, 10% $CO_2$, 5 W LED light (400–800 nm) | CO: 58 | *App. Catal. B-Environ.* **2020**, *260*, 118208 |
| In-MOF@TP-TA | 2 mL $H_2O$, 300 W Xe lamp | CO: 25.0<br>$CH_4$: 11.67 | *Chem. Eng. J.* **2022**, *446*, 137011 |
| Ni@6MOF/BVO | 5 mL $H_2O$, 300 W Xe lamp | CO: 44.5 | *Adv. Mater.* **2022**, *34*, e2205303 |
| $In_2O_3$/BiOI | 100 mL $H_2O$, 10 mL TEOA, 300 W Xe lamp | CO: 11.9 | *J. $CO_2$ Util.* **2022**, *65*, 102220 |

## SECTION S4. Supplemental references


1. Z. Duan, Y. Wang, S. Bian, D. Liu, Y. Zhang, X. Zhang, R. He, J. Wang, G. Qu, P. K. Chu and X. Yu, *Nanoscale*, 2022, **14**, 2599-2604.
2. T. He, X. Xu, B. Ni, H. Wang, Y. Long, W. Hu and X. Wang, *Nanoscale*, 2017, **9**, 19209-19215.
3. Z. Huo, Z. Duan, X. Feng, H. Wang, H. Huang, X. Fan, R. He, X. F. Yu and J. Wang, *Small*, 2024, **20**, e2402483.
4. Z. Duan, Q. Tong, X. Feng, H. Wang, Y. Yang, J. Wang, D. Liu, H. Bian, R. Li and Y. Yang, *Inorg. Chem.*, 2025, **64**, 14759-14766.
5. Y. Wang, X. Zhang, Y. Sun, K. Chen, H. Zhao, Q. Lin, R. Li and J. Li, *Appl. Catal. B-Environ. Energy*, 2025, **378**, 125568.